4-25-2022

Real-Time Measurement of Parametric Influences on the Refractive Index and Length Changes in Silica Optical Fibers

Sohel Rana
Boise State University

Austin Fleming
Idaho National Laboratory

Harish Subbaraman
Boise State University

Nirmala Kandadai
Boise State University

Research Article | Vol. 30, No. 9 / 25 Apr 2022 / Optics Express 15659
Optics EXPRESS

Real-time measurement of parametric influences on the refractive index and length changes in silica optical fibers

SOHEL RANA,[1,2] AUSTIN FLEMING,[1] HARISH SUBBARAMAN,[2] AND NIRMALA KANDADAI[2,*]

[1]Measurement Science Department, Idaho National Laboratory, 1955 N Fremont Ave, Idaho Falls, ID 83415, USA
[2]Department of Electrical and Computer Engineering, Boise State University, Boise, ID 83725, USA
*nirmalakandadai@boisestate.edu

Abstract: In this paper, we present a simple cascaded Fabry-Perot interferometer (FPI) that can be used to measure in real-time the refractive index (RI) and length variation in silica optical fibers caused due to external physical parameters, such as temperature, strain, and radiation. As a proof-of-concept, we experimentally demonstrate real-time monitoring of temperature effects on the RI and length and measure the thermo-optic coefficient (TOC) and thermal expansion coefficient (TEC) by using the cascaded FPI within a temperature range of 21–486°C. The experimental results provide a TEC of 5.53×10^{-7}/°C and TOC of 4.28×10^{-6}/°C within the specified temperature range. Such a simple cascaded FPI structure will enable the design of optical sensors to correct for measurement errors by understanding the change in RI and length of optical fiber caused by environment parameters.

1. Introduction

Real-time monitoring of refractive index (RI) and length variation in an optical fiber induced by environmental parameters, such as temperature, strain, pressure, and radiation has been of great importance in characterizing optical devices since the birth of optical fibers [1–3]. In practice, the sensors based on optical fibers can be calibrated with the knowledge of parametric influence on the RI and length changes. For a widespread application, namely real-time temperature sensing, fiber optic sensors such as fiber Bragg gratings (FBGs) and Fabry-Perot interferometer (FPI), have been applied to measure the change in RI with temperature [3–5]. However, the thermo-optic coefficient (TOC) which is a measure of the RI change as a function of temperature maybe positive or negative, and this depends on two processes which are driven by change in temperature [6]. The density of an optical fiber may decrease with increasing temperature because of thermal expansion. Reduction in density leads to negative RI [7]. However, heating the optical fiber polarizes it significantly and increases RI [6,8]. Although these two individual mechanisms can lead to positive or negative RI, the net effect has shown to be positive for silica optical fibers [9]. The TEC, which provides the variation of length with temperature at constant pressure, is always positive for silica optical fiber and almost one order of magnitude smaller than the TOC. Several methods have proven to be effective for measuring RI and hence the TOC; these include interferometric [10,11] and prismatic methods [12,13]. However, prismatic methods are non-fiber methods, and their direct application for TOC measurement may provide inaccurate results for optical fiber. RI due to temperature and hence the TOC can also be measured by direct techniques such as refracted near-field, multiwavelength interferometry, computerized tomography, differential interference-contrast microscopy, and quantitative phase microscopy [14]. However, some of these measurements require the cut of the fiber (destructive analysis) and may not provide real-time changes of RI due to the post recovery. Recent years FBGs, FPIs, and

#450528 https://doi.org/10.1364/OE.450528
Journal © 2022 Received 5 Dec 2021; revised 16 Mar 2022; accepted 21 Mar 2022; published 22 Apr 2022

Optics EXPRESS

combination of them have been used to measure the TOC and the TEC in real-time of optical fibers; however, fabrication of FBGs, inclusion of femtosecond(fs) laser, etching, and so on make sensor's structure complex and increase the cost [3–5]. Moreover, FBG-based techniques may have temperature limitation due to the dependence on temperature for grating stability. So far, the reported values for the TOC of silica-based optical fibers using existing methods are between 3×10^{-6}/°C and 2.37×10^{-5}/°C at different temperatures and wavelengths [3–5, 12,15,16]. While there are several techniques for real-time monitoring of TEC and TOC of silica optical fibers currently exist, an optical structure having the following advantages such as ease of fabrication, ability to survive in harsh environment, and cost-effective are yet to be expected.

Very recent in our modeling work, a cascaded FPI to measure the RI and length due to mixed radiation has been reported [17]. In this paper, as a proof-of-concept, we experimentally demonstrate real-time monitoring of temperature effects on the RI and length and measure TEC and TOC using the cascaded FPI. The proposed structure consists of an extrinsic FPI (EFPI) and an intrinsic FPI (IFPI) as a way to accurately measure the TOC and TEC for silica optical fibers within a temperature range of 21–486°C. The EFPI can be used to measure the physical cavity length since it is air filled, and the RI of air is almost invariant with temperature. On the other hand, temperature alters the RI and the length of the IFPI for being a solid cavity made of pure silica. Because the TEC of a silica capillary tube and pure silica fiber is same, it is possible to extract the RI change from IFPI by using length in the EFPI. Due to differences in the cavities, air versus silica, the Fabry-Perot responses would be different. To separate individual signals for each cavity from the mixed signal of cascaded FPI, we apply a fast Fourier transform (FFT) algorithm to convert the wavelength domain signal to the spatial-frequency domain and then use Butterworth filters. Inverse Fourier transform is applied on the filtered signals to reconstruct the individual signal again in wavelength domain. Since the proposed structure is made of silica capillary and optical fiber, simple cleaving and splicing processes are required for the fabrication. Moreover, for being all silica structure, the cascaded FPI structure can be applied in extreme radiation environment to determine the effect of other parametric influences such as pressure and radiation as these effects are directly coupled to the RI and length changes.

2. Fabrication and working principle of cascaded FPI

Our design architecture consists of an EFPI and an IFPI as shown in Fig. 1(a), where L_1 and L_2 denote the cavity length for the EFPI and the IFPI, respectively. The interface M_1 between the lead in SMF-28 fiber and the capillary and the interface, M_2, between the capillary and the coreless (CL) silica fiber constitute the EFPI (first cavity/air cavity). On the other hand, the interface M_2 and M_3 between the CL fiber and air constitute the IFPI (second cavity/silica cavity). One additional cavity is called the hybrid cavity (third cavity/air-silica cavity), and it forms between interfaces M_1 and M_3. These interfaces work as mirrors to reflect light. In this cascaded FPI, the incoming light that reflects from interfaces M_1, M_2, and M_3 are I_1, I_2, and I_3, respectively. Then total reflection of light based on the three-beam interference can be expressed by [18] :

$$I = I_1 + I_2 + I_3 + 2\sqrt{I_1 I_2}\cos(\varphi_{air}) + 2\sqrt{I_2 I_3}\cos(\varphi_{silica}) + 2\sqrt{I_1 I_3}\cos(\varphi_{air-silica}) \quad (1)$$

where $\varphi_{air} = \frac{4\pi n_1 L_1}{\lambda}$, $\varphi_{silica} = \frac{4\pi n_2 L_2}{\lambda}$, and $\varphi_{air-silica} = \frac{4\pi}{\lambda}(n_1 L_1 + n_2 L_2)$ are the phase shift of the air cavity (first cavity), silica cavity (second cavity), and hybrid cavity, respectively. Also, here n_1 and n_2 are the RI of the air and silica optical fiber, respectively. In order to fabricate the cascaded FPI, we applied simple cleaving and splicing processes. We used SMF-28 single-mode fiber (SMF-28e+, Corning) as the lead-in fiber and capillary tubes with inner diameters of 39.2 µm (TSP040150) from Polymicro Technologies to construct the EFPI. As a first step, we cleaved the SMF-28, the capillary tube, and the coreless (CL) fiber using cleaving tool (CT101/102, Fujikura) [Fig. 1(b)] and then fusion spliced the SMF-28 with the capillary tube using a fusion

Optics EXPRESS

splicer (70S+ fusion splicer, Fujikura) [Fig. 1(c)]. Next, a linear stage in conjunction with the cleaving tool was used to cleave the spliced capillary at a distance of 148 μm from the splicing point [Fig. 1(c)]. A CL fiber from Thorlabs was cleaved and spliced with the capillary tube to complete the EFPI [Fig. 1(d)]. The CL fiber was chosen for the IFPI in order to obtain information about the pure silica optical fiber. Then we cleaved the CL fiber at a distance of 323 μm from the splicing point of the capillary and CL fiber to construct the IFPI [Fig. 1(d)]. The lengths L_1=148 μm and L_1=323 μm were chosen in such a way so that the signal peak of one cavity does not overlap or position very close to the other cavity peaks in the spatial frequency domain. A microscopic image of the fabricated cascaded FPI is shown in Fig. 1(e) The measured cavity lengths were found to be L_1=148 μm and L_1=323 μm. The baseline interference spectrum of the cascaded FPI as recorded by an optical sensing instrument (Hyperion si255, Luna) is shown in Fig. 2(a). To retrieve the spectral response of each cavity, optical-frequency-domain signal processing was adopted. First, the recorded signal from the interrogator was converted from the wavelength domain to a wavenumber domain ($wavenumber = \frac{2\pi}{\lambda}$). Because the spectrum based on wavenumber is not evenly spaced, a cubic spline was performed. Then FFT was applied on this modified spectrum, and the corresponding spatial-frequency domain distribution is shown in Fig. 2(b). This can also be done using non-uniform Fast Fourier Transform (NUFFT) and we verified it (not shown in this paper). There, the three dominant peaks, namely Peak1, Peak2, and Peak3, correspond to three cavities. Peak1 corresponds to the air cavity, which was confirmed by calculating the spatial frequency $\left(\frac{2n_1L_1}{\lambda_1\lambda_2}\right)$ at room temperature where λ_1 and λ_2 are the wavelengths of adjacent peaks or dips in the reflection spectrum of each cavity. In a similar way, Peak 2 and Peak 3 belong to the silica and hybrid cavities, respectively. The measured spatial frequencies of the air cavity and the silica cavities were found to be 0.125 nm^{-1} (Peak1) and 0.39375 nm^{-1} (Peak2), respectively, which correspond to a cavity length of ~147 and ~321 μm. These calculated cavity lengths are close to the actual measured cavity lengths. To extract the signals for each cavity from the total reflection spectrum, two bandpass filters were used. The interference spectrum of the air cavity can be obtained by filtering the total spectrum using

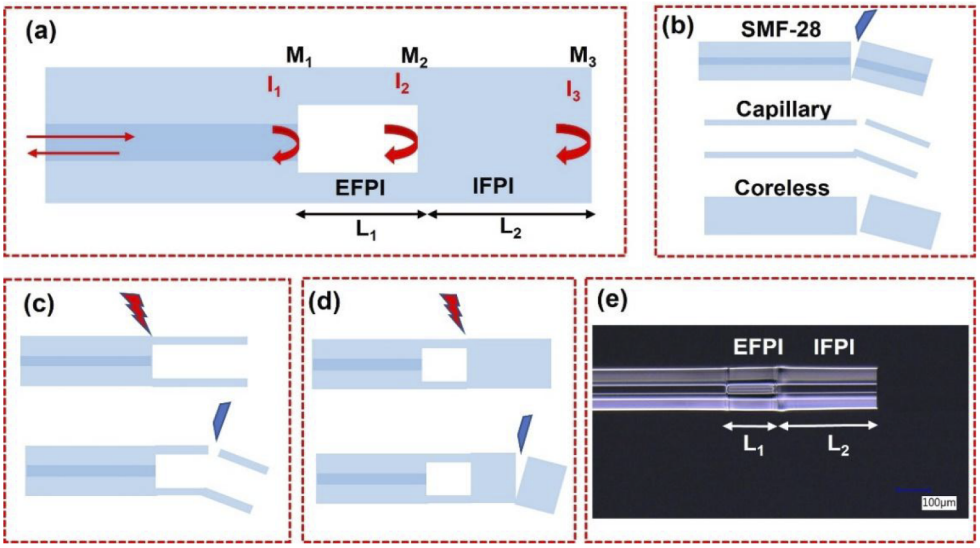

Fig. 1. Schematic and fabrication of cascaded FPI: (a) schematic of cascaded FPI, (b) cleaving of required fibers and capillary, (c, d) splicing and cleaving steps, and (e) microscopic image of fabricated cascaded FPI.

Optics EXPRESS

a bandpass filter centered on Peak1 and for the silica cavity centered on Peak2. Then inverse Fourier transform was applied on these filtered signals to reconstruct the spectra for each cavity back into the wavelength domain. The retrieved spectra for the air and the silica cavities are shown in Figs. 2(c) and 2(d), respectively. The free-spectrum range (FSR), which is defined as the spectral distance between two adjacent peaks or dips was found to be ~8 and ~2.54 nm for the air cavity and the silica cavity, respectively, which is consistent with their cavity lengths.

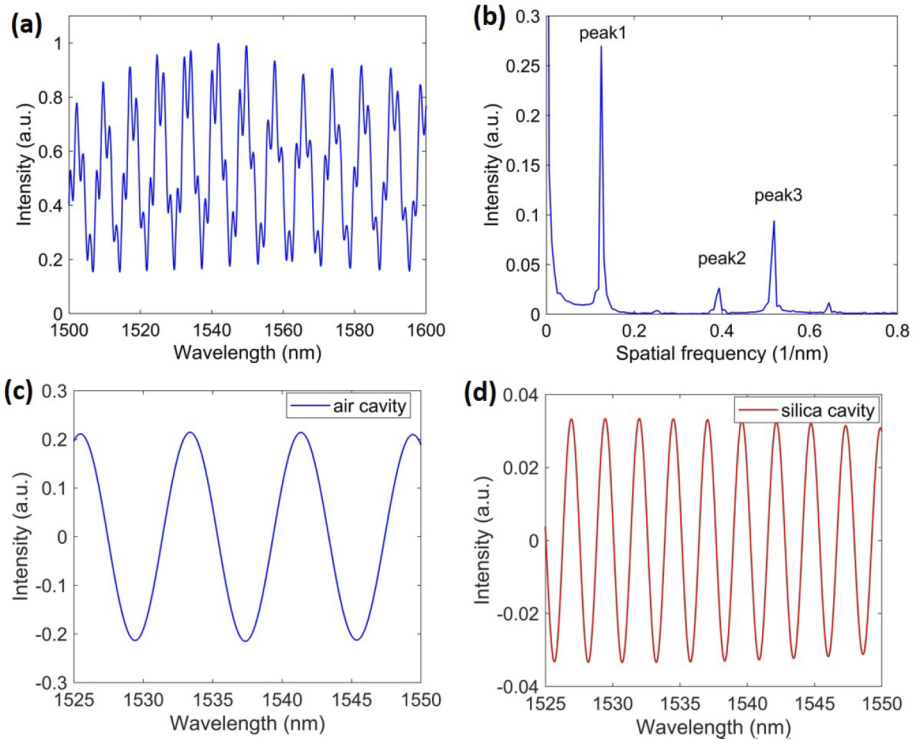

Fig. 2. Spectral response of fabricated cascaded FPI: (a) total reflection spectrum, (b) optical frequency domain distribution of the total reflection spectrum, (c) reconstructed cavity length of EFPI, and (d) reconstructed cavity length of IFPI.

3. Thermal effects on cavities

With the basic specifications of the two cavities determined and baseline spectrum measured, we next studied the effect of temperature on both cavities. In order to measure the TEC and TOC, the fabricated cascaded FPI was placed inside a tube furnace with endcaps to ensure no air flow. A k-type thermocouple was also placed very close to the FPI to measure the temperature at the location of the FPI in the furnace to improve measurement accuracy. A schematic of the measurement setup is shown in Fig. 3. The temperature of the furnace was increased from ambient to 486°C with a ramp rate of 5°C/min. The total reflection signal was recorded at different temperatures using the optical sensing instrument (Hyperion si255, Luna). For each measurement, a hold time of 30 minutes was used to stabilize the temperature before recording data. The recorded data were then analyzed to reconstruct the signal for each cavity discussed in Section 2. The air cavity shows a thermal expansion only with temperature because it is made of silica capillary tubes. On the other hand, the silica cavity is an IFPI, and temperature changes both the RI and the length of the cavity. These properties from both cavities can be used to measure TEC and the TOC in real time.

Optics EXPRESS

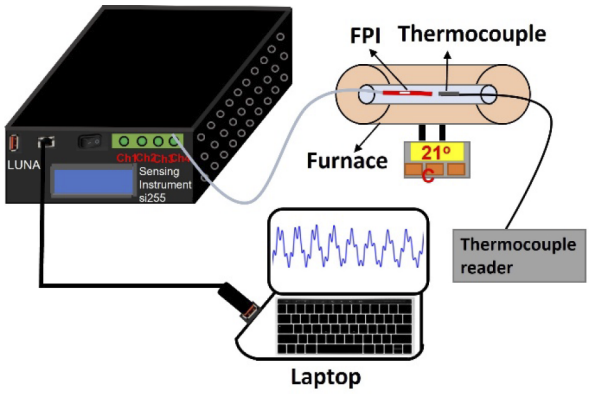

Fig. 3. Experimental setup to record signal at different temperatures.

3.1. Thermal expansion coefficient

The TEC of an optical fiber plays a key role in optical fiber sensing technology. Although the TEC ($\sim 5.5 \times 10^{-7}/^{\circ}\mathrm{C}$) is well defined for fused silica sample, it changes for optical fiber with temperature [3,5]. To monitor the TEC in real-time, the fabricated cascaded FPI was used. Since the EFPI is hollow and the change in air RI with temperature is very small, which calculated by the following expression [19]

$$n_1 = 1 + \frac{2.8793 \times 10^{-9} \times P}{1 + 0.003661 \times T} \tag{2}$$

where P is the absolute pressure and T is the operating temperature. In this equation, the change in RI of air with temperature is negligible because the second term in the right-hand side remains almost constant by the increased temperature and temperature-induced increased pressure because the air is sealed in a nearly constant-volume cavity. Because the spectrum of an FPI is governed by the optical length of the cavity, and for the air cavity, the effect of RI is so small as to be neglected. The length expansion of the cavity is the parameter expected to be dominant. The inner diameter of the capillary tube is of 39.2 μm, which leaves a 42.9 μm wall thickness, which experiences a length expansion. The response of air cavity at different temperatures were recorded from the experiment described above. Then the cavity length of the air cavity was calculated from the measured spectrum using the following two peak methods [20]:

$$L_1 = \frac{\lambda_1 \lambda_2}{2n_1(\lambda_2 - \lambda_1)} \tag{3}$$

where λ_1 and λ_2 are the wavelengths of adjacent peaks or dips in the reflection spectrum.

Because the spectrum of the air cavity contains many peaks, to retrieve the cavity length, the cavity length for each set of adjacent peaks were calculated and then averaging that. We obtained a cavity length of ~147 μm at room temperature from the measured spectrum using the Eq. (3). The spectra of the air cavity at six temperatures – 21, 100, 197, 291, 388, and 486°C are shown in Fig. 4. Because this is an air cavity, the dip/peak wavelength shifts a small amount with temperature. As temperature expands the cavity length, the interference spectra get closer.

The cavity length at each temperature was calculated from each spectrum using the Eq. (3). Then these cavity lengths at each temperature were plotted against temperature to find the TEC, which is shown in Fig. 5. We performed the experiment twice to confirm the repeatability of the cascaded FPI structure. The solid red circles are the mean experimental data at each temperature, and the solid blue line shows the linear fitting of these data. The error bar in Fig. 5 indicates the

Optics EXPRESS

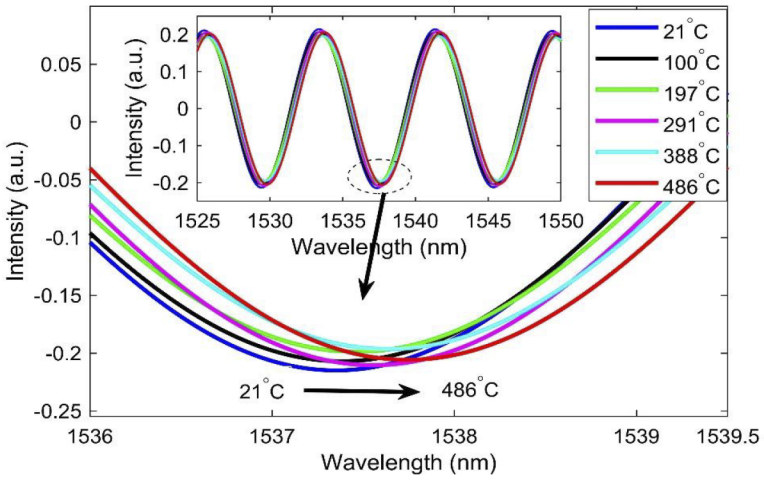

Fig. 4. Measured spectra of the air cavity at different temperatures.

standard deviation from the mean values. It is seen that the data follow a linear trend upward to the specified temperature range with a linear fit of R^2 of 0.9892 and root mean square error (RMSE) of 0.001678. The obtained TEC from these data was found to be 5.53×10^{-7}/°C, which is in good agreement with literature values. The TEC and the temperature as a function of heating time can be seen in Supplement 1. Once the air-cavity length is known for each temperature, then the length expansion (α) can be represented as

$$\alpha = \frac{L_{a,T} - L_{a,i}}{L_{a,i}} \tag{4}$$

where $L_{a,i}$ is the initial air-cavity length at room temperature, and $L_{a,T}$ is the final air-cavity length at any temperature. Please note that the optical-cavity length and the physical-cavity length are same for the air cavity because air has an RI of 1.

3.2. Thermo-optic coefficient (TOC)

The TOC is the change in RI with temperature at constant pressure. To measure the TOC real-time, the same experimental setup of Fig. 3 was used, and the experiment was repeated twice. Because the IFPI is made of coreless pure silica fiber, temperature alters both the RI and the cavity length. Therefore, the spectrum of the silica cavity contains information about both the RI and the length of the cavity. The spectrum of the silica cavity at different temperatures is shown in Fig. 6. It is seen that the spectral position changes continuously with temperature. Since the silica capillary tube and the silica cavity both are made of silica and for being very close proximity of both cavities to each other, it is expected that both the cavities will experience the same length expansion. Please note that length expansion is a relative value and always defined as the change in physical length with respect to the initial physical length. The silica cavity length expansion (α) can be deduced by using the Eq. (5),

$$\frac{L_{Si,T} - L_{Si,i}}{L_{Si,i}} = \alpha = \frac{L_{a,T} - L_{a,i}}{L_{a,i}} \tag{5}$$

where $L_{Si,i}$ is the initial cavity length at room temperature and $L_{Si,T}$ is the final cavity length of the silica cavity at any temperature. Next, the silica-cavity length at any temperature can be

Optics EXPRESS

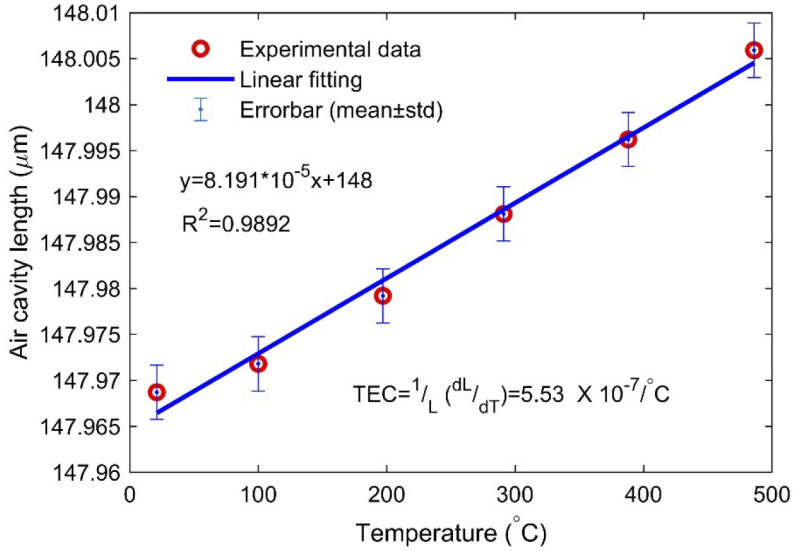

Fig. 5. Measured air-cavity length as a function of applied temperature.

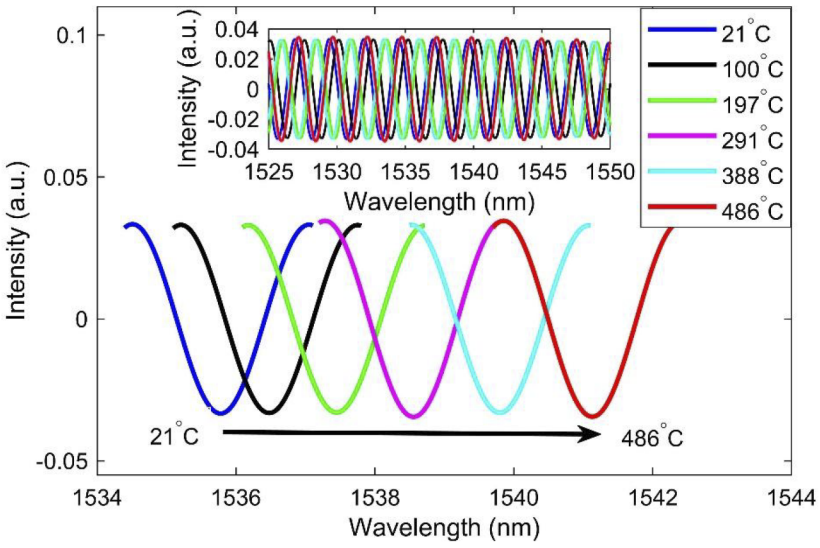

Fig. 6. Measured spectra of the silica cavity at different temperatures.

Optics EXPRESS

calculated by using the below expression

$$L_{Si,T} = L_{Si,i} + L_{Si,i} \times \alpha. \tag{6}$$

Because the silica-cavity length, $L_{Si,i}$ at room temperature, and α are known, the cavity length $L_{Si,T}$ can be calculated from Eq. (6). The optical silica-cavity length ($L_{Si,opt}$) is also known from the measured spectrum of the silica cavity. However, $L_{Si,opt} = n_{2f} \times L_{Si,T}$ where n_{2f} is the final RI of silica cavity with temperature, which can be easily deduced. The variation of RI of silica optical fiber with temperature is shown in Fig. 7. The solid red circles are the mean experimental data, and the solid blue line shows the linear fitting of these data. The error bar in Fig. 7 indicates the standard deviation from the mean values. It is seen that the data follow a linear trend upward to the specified temperature range with a linear fit of R^2 of 0.9914 and root mean square error (RMSE) of 0.0001134.The obtained TOC from these data were found to be 4.28×10^{-6}/°C, which is in a good agreement with literature values reported in Refs [3–5,12,15,16]. The TOC and the temperature as a function of heating time can be seen in Supplement 1.

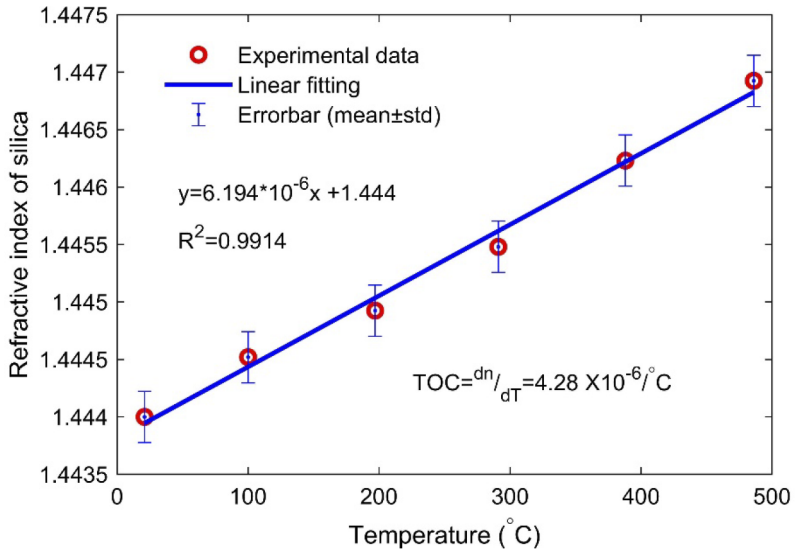

Fig. 7. Measured refractive index of silica optical fiber as a function of applied temperature.

4. Discussions and applications

The change in length and RI of optical fiber has been measured using a simple structure, based on EFPI and IFPI. Because only silica material is used to construct the structure, it is possible to use this structure at high temperatures, unlike FBGs where grating stability depends on the operating temperature. Through this work, we have demonstrated the potential of our simple cascaded FPI structure in accurately determining the RI and length change due to an applied stimulus. *In situ* measurement of RI and length can find a potential application in the nuclear environment. Incoming radiation (gamma ray, neutron fluence, or both) changes the optical as well as the mechanical properties of optical fibers [21–24]. Radiation-induced attenuation (RIA) significantly affects the signal strength by creating different types of defects [25,26] whereas radiation-induced compaction (RIC) causes signal drift by compacting the material [22,27]. For optical-fiber sensors, it is the RIC over the RIA which causes temperature-measurement errors in the nuclear environment, thanks to radiation-hardened optical fibers [28,29]. If the RIC is known, it is possible to calculate the RI induced by RIC by using well-established Lorentz-Lorenz relation

Optics EXPRESS

[30,31] and point dipole theory [32]. However, these methods only consider the RIC-induced RI change. It has also been shown that RIA, in addition to RIC, causes signal drift [33]. As a result, RIA-induced RI change must also be known to understand radiation-induced signal drift. While Kramers-Kronig relation can be used to assess the change in RI from RIA [34,35], it requires the full spectrum in a wide frequency range for which dose-dependent data are not available. Besides RIA and RIC, there may be other phenomena, like dopant diffusion, stress relaxation of fiber, temperature, and so on, which alter the RI and the length of the optical fiber [36,37] . Moreover, their individual effects on the RI and the length of the optical fiber may be different from their combined effects. Online measurement may provide the change in RI and length of optical fiber caused by any specific phenomena to which the fiber is subjected, including RIC, RIA, dopant diffusion, and temperatures. Once the individual contribution of RI and length on signal drift are known, it is possible to model an optimized sensor design to correct radiation-induced signal drift while measuring other physical parameters. Because the proposed cascaded FPI can make online measurements of the RI and length changes, it has the potential to be used in high pressure or radiation environments to compensate for signal drift.

5. Summary

An online measurement of both the RI and length of an optical fiber, using a simple cascaded FPI under different temperatures, has been performed. In the cascaded FPI, the first cavity is the air cavity, which has been used to measure the length expansion because the RI of air shows no significant change with temperature. Next, this length-expansion has been applied to the silica cavity (i.e., the second cavity) to measure the RI of this cavity. Frequency-domain optical-signal processing has been adopted to extract signals for each cavity. This simple structure, based on cascaded FPI may find application in the nuclear environment, where radiation-induced change in RI and the length of optical fiber is of utmost importance to reduce the radiation-induced signal drift's causing measurement error in temperature monitoring when fiber-optic sensors are dedicated as temperature sensors.

Funding. Idaho Operations Office, U.S. Department of Energy (DE-AC07-05ID14517).

Disclosures. The authors declare no conflicts of interest. This work was supported in part through the Department of Energy Advanced Sensors and Instrumentation program. The views and opinions of authors expressed herein do not necessarily state or reflect those of the U.S. Government or any agency thereof.

Data availability. Data underlying the results presented in this paper are not publicly available at this time but may be obtained from the corresponding author upon reasonable request.

Supplemental document. See Supplement 1 for supporting content.

References

1. M. Cavillon, P. D. Dragic, and J. Ballato, "Additivity of the coefficient of thermal expansion in silicate optical fibers," Opt. Lett. **42**(18), 3650–3653 (2017).
2. E. D. Palik, " in *Handbook of Optical Constants of Solids* (Academic Press, 1997), Chap.3.
3. H. Gao, Y. Jiang, Y. Cui, L. Zhang, J. Jia, and L. Jiang, "Investigation on the thermo-optic coefficient of silica fiber within a wide temperature range," J. Lightwave Technol. **36**(24), 5881–5886 (2018).
4. G. Adamovsky, S. F. Lyuksyutov, J. R. Mackey, B. M. Floyd, U. Abeywickrema, I. Fedin, and M. Rackaitis, "Peculiarities of thermo-optic coefficient under different temperature regimes in optical fibers containing fiber Bragg gratings," Opt. Commun. **285**(5), 766–773 (2012).
5. L. Li, D. Lv, M. Yang, L. Xiong, and J. Luo, "A IR-femtosecond laser hybrid sensor to measure the thermal expansion and thermo-optical coefficient of silica-based FBG at high temperatures," Sensors **18**(2), 359 (2018).
6. L. Prod'Homme, "A new approach to the thermal change in the refractive index of glasses," Phys. Chem. Glasses **1**, 119 (1960).
7. E. Talebian and M. Talebian, "A general review on the derivation of Clausius–Mossotti relation," Optik **124**(16), 2324–2326 (2013).
8. T. Bååk, "Thermal coefficient of refractive index of optical glasses-," J. Opt. Soc. Am. **59**(7), 851–857 (1969).
9. M. J. O'Dwyer, C.-C. Ye, S. W. James, and R. P. Tatam, "Thermal dependence of the strain response of optical fibre Bragg gratings," Meas. Sci. Technol. **15**(8), 1607–1613 (2004).

Optics EXPRESS

10. R. M. Waxler and G. W. Cleek, "Refractive indices of fused silica at low temperatures," J. Res. Natl. Bur. Stand., Sect. A **75A**(4), 279–281 (1971).
11. P.-E. Dupouy, M. Büchner, P. Paquier, G. Trénec, and J. Vigué, "Interferometric measurement of the temperature dependence of an index of refraction: application to fused silica," Appl. Opt. **49**(4), 678–682 (2010).
12. J. H. Wray and J. T. Neu, "Refractive index of several glasses as a function of wavelength and temperature," J. Opt. Soc. Am. **59**(6), 774–776 (1969).
13. I. H. Malitson, "Interspecimen comparison of the refractive index of fused silica," J. Opt. Soc. Am. **55**(10), 1205–1209 (1965).
14. D. Marcuse, *Principles of optical fiber measurements*; Elsevier Science, Amsterdam, The Netherlands, 2012.
15. N. Yang, Q. Qiu, J. Su, and S. Shi, "Research on the temperature characteristics of optical fiber refractive index," Optik **125**(19), 5813–5815 (2014).
16. Y. Guo, Z.-Y. Wang, Q. Qiu, J. Su, Y. Wang, S. Shi, and Z. Yu, "Theoretical and experimental investigations on the temperature dependence of the refractive index of amorphous silica," J. Non-Cryst. Solids **429**, 198–201 (2015).
17. S. Rana, A. Fleming, H. Subbaraman, and N. Kandadai, "Active compensation of radiation effects on optical fibers for sensing applications," Sensors **21**(24), 8193 (2021).
18. Y. Wu, Y. Zhang, J. Wu, and P. Yuan, "Fiber-optic hybrid-structured Fabry–Perot interferometer based on large lateral offset splicing for simultaneous measurement of strain and temperature," J. Lightwave Technol. **35**(19), 4311–4315 (2017).
19. M. Deng, C.-P. Tang, T. Zhu, Y.-J. Rao, L.-C. Xu, and M. Han, "Refractive index measurement using photonic crystal fiber-based Fabry-Perot interferometer," Appl. Opt. **49**(9), 1593–1598 (2010).
20. Y. Jiang, "High-resolution interrogation technique for fiber optic extrinsic Fabry-Perot interferometric sensors by the peak-to-peak method," Appl. Opt. **47**(7), 925–932 (2008).
21. G. Cheymol, L. Remy, A. Gusarov, D. Kinet, P. Mégret, G. Laffont, T. Blanchet, A. Morana, E. Marin, and S. Girard, "study of fiber Bragg grating samples exposed to high fast neutron fluences," IEEE Trans. Nucl. Sci. **65**(9), 2494–2501 (2018).
22. L. Remy, G. Cheymol, A. Gusarov, A. Morana, E. Marin, and S. Girard, "Compaction in optical fibres and fibre Bragg gratings under nuclear reactor high neutron and gamma fluence," IEEE Trans. Nucl. Sci. **63**(4), 2317–2322 (2016).
23. S. Girard, C. Marcandella, A. Morana, J. Perisse, D. D. Francesca, P. Paillet, J.- Macé, A. Boukenter, M. Léon, M. Gaillardin, N. Richard, M. Raine, S. Agnello, M. Cannas, and Y. Ouerdane, "Combined high dose and temperature radiation effects on multimode silica-based optical fibers," IEEE Trans. Nucl. Sci. **60**(6), 4305–4313 (2013).
24. C. M. Petrie, A. Birri, and T. E. Blue, "High-dose temperature-dependent neutron irradiation effects on the optical transmission and dimensional stability of amorphous fused silica," J. Non-Cryst. Solids **525**, 119668 (2019).
25. S. Girard, J. Kuhnhenn, A. Gusarov, B. Brichard, M. Van Uffelen, Y. Ouerdane, A. Boukenter, and C. Marcandella, "Radiation effects on silica-based optical fibers: recent advances and future challenges," IEEE Trans. Nucl. Sci. **60**(3), 2015–2036 (2013).
26. S. Girard, A. Alessi, N. Richard, L. Martin-Samos, V. De Michele, L. Giacomazzi, S. Agnello, D. D. Francesca, A. Morana, B. Winkler, I. Reghioua, P. Paillet, M. Cannas, T. Robin, A. Boukenter, and Y. Ouerdane, "Overview of radiation induced point defects in silica-based optical fibers," Reviews in Physics **4**, 100032 (2019).
27. W. Primak, "Mechanism for the radiation compaction of vitreous silica," J. Appl. Phys. **43**(6), 2745–2754 (1972).
28. G. Berkovic, S. Zilberman, E. Shafir, Y. London, M. Dadon, M. Alefe, K. Ben Meir, A. Krakovich, and T. Makmal, "Characterization of radiation hardened fibers in a research grade nuclear reactor," in *Micro-Structured and Specialty Optical Fibres VII*, P. Peterka, K. Kalli, and A. Mendez, eds., (SPIE, 2021), p. 23.
29. M. A. S. Zaghloul, M. Wang, S. Huang, C. Hnatovsky, D. Grobnic, S. Mihailov, M.-J. Li, D. Carpenter, L.-W. Hu, J. Daw, G. Laffont, S. Nehr, and K. P. Chen, "Radiation resistant fiber Bragg grating in random air-line fibers for sensing applications in nuclear reactor cores," Opt. Express **26**(9), 11775–11786 (2018).
30. H. Kakiuchida, K. Saito, and A. J. Ikushima, "Refractive Index, Density and Polarizability of Silica Glass with Various Fictive Temperatures," Jpn. J. Appl. Phys. **43**(No. 6A), L743–L745 (2004).
31. A. Alessi, S. Agnello, S. Grandi, A. Parlato, and F. M. Gelardi, "Refractive index change dependence on Ge(1) defects in γ-irradiated Ge-doped silica," Phys. Rev. B **80**(1), 014103 (2009).
32. N. Kitamura, Y. Toguchi, S. Funo, H. Yamashita, and M. Kinoshita, "Refractive index of densified silica glass," J. Non-Cryst. Solids **159**(3), 241–245 (1993).
33. A. Morana, S. Girard, E. Marin, C. Marcandella, P. Paillet, J. Périsse, J.-R. Macé, A. Boukenter, M. Cannas, and Y. Ouerdane, "Radiation tolerant fiber Bragg gratings for high temperature monitoring at MGy dose levels," Opt. Lett. **39**(18), 5313–5316 (2014).
34. S. Kher, S. Chaubey, S. M. Oak, and A. Gusarov, "Measurement of γ-radiation induced refractive index changes in B/Ge doped fiber using LPGs," IEEE Photonics Technol. Lett. **25**(21), 2070–2073 (2013).
35. D. C. Hutchings, M. Sheik-Bahae, D. J. Hagan, and E. W. Van Stryland, "Kramers-Krönig relations in nonlinear optics," Opt. Quantum Electron. **24**(1), 1–30 (1992).
36. D. Grobnic, C. W. Smelser, S. J. Mihailov, and R. B. Walker, "Long-term thermal stability tests at 1000 °C of silica fibre Bragg gratings made with ultrafast laser radiation," Meas. Sci. Technol. **17**(5), 1009–1013 (2006).
37. D. Grobnic, C. Hnatovsky, S. Dedyulin, R. B. Walker, H. Ding, and S. J. Mihailov, "Fiber Bragg grating wavelength drift in long-term high temperature annealing," Sensors **21**(4), 1454 (2021).